Solar Energy Materials & Solar Cells 271 (2024) 112875

Contents lists available at ScienceDirect

Solar Energy Materials and Solar Cells

journal homepage: www.elsevier.com/locate/solmat

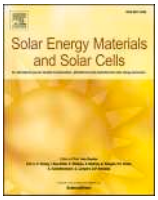

Zirconium doped indium oxide thin films as transparent electrodes for photovoltaic applications

Melanie Micali [a,b,e,*], Andrea Lo Mastro [a,b], Fiorella Tringali [a,b], Marco Leonardi [c,d], Salvatore Lombardo [c], Giuseppe Bengasi [d], Claudio Colletti [d], Marina Foti [d], Esther Alarcón Lladó [e,f], Maria Miritello [b], Giorgia Franzò [b], Antonio Terrasi [a,b]

[a] Dipartimento di Fisica e Astronomia "Ettore Majorana", Università di Catania, via S. Sofia 64, I-95123, Catania, Italy
[b] IMM-CNR, Sede Catania (Università), via S. Sofia 64, 95123, Catania, Italy
[c] Istituto per la Microelettronica e Microsistemi- Consiglio Nazionale delle Ricerche, Zona Industriale, Ottava Strada n.5, 95121, Catania, Italy
[d] 3SUN-ENEL Green Power, Contrada Blocco Torrazze sn- Z.I., 95121, Catania, Italy
[e] AMOLF Physics of Functional Matter, Science Park 104, NL1098XG, Amsterdam, the Netherlands
[f] Van 't Hoff Institute for Molecular Sciences, University of Amsterdam, Science Park 904, 1090 GD, Amsterdam, the Netherlands

ARTICLE INFO

Keywords:
TCO
Photovoltaics
Transparent electrodes
Sputtering

ABSTRACT

In this work we report on ultra-thin Zirconium doped In_2O_3 transparent conductive films grown at room temperature via RF-Magnetron co-sputtering. Samples from 15 nm to 90 nm thick, and low Zr atomic concentration (0.6–0.9 at.%), were annealed at T = 200 °C after the deposition. The phase-transition from amorphous to crystalline, confirmed by XRD measurements, leads to an improvement of both electrical and optical properties. The thinnest film (15 nm) shows electrical resistivity as low as 5×10^{-4} Ωcm, with carrier mobility of 20 $cm^2V^{-1}s^{-1}$, and optical transmittance up to 80 % in visible and near-infrared range. IZrO electrode performances were tested through external quantum efficiency (EQE) measurements on a semi-finite Silicon Heterojunction bifacial solar cell. The EQE values for 90 nm thick film are comparable to that of standard ITO when IZrO films are implemented as front electrodes. These results suggest that ultra-thin IZrO films may be successfully used to reduce costs and the amount of Indium used in Indium-based transparent conductive oxide layers for solar cells.

1. Introduction

Transparent electrodes are a necessary component in many modern devices such as solar cells, electrochromic glass, flexible OLED, low emissivity windows, touch panel displays, and electromagnetic shielding. Traditionally, this role has been well served by Transparent Conductive Oxides (TCO), characterized by good transmittance to visible (VIS) and near-infrared (NIR) light and low electrical resistivity. However, the demand has extended beyond conductivity and transparency, for which indeed higher performances are required, but it also includes long-term stability, low surface roughness, well-defined work function, high mechanical flexibility, reliability and robustness upon thermal annealing processes, abundance of raw materials and low fabrication costs [1–4]. Within this class of materials, Indium Tin Oxide (ITO) is mostly favored because it is an n-type, highly degenerate, wide bandgap semiconductor that offers the highest available transmissivity for visible light combined with the lowest electrical resistivity. However, it also presents multiple drawbacks such as high cost due to scarcity of Indium, low NIR transmittance, brittleness with the occurrence of cracks under mechanical stress, and limited application in flexible optoelectronic devices. The sputtering process for ITO coating is typically carried out at temperatures around 200 °C and it results in sheet resistances below 20 Ω/□ at 90 % transmittance; whereas, when a flexible plastic substrate is used, ITO is preferably deposited at lower temperatures to prevent any damage to the substrate, with the corresponding increase of the sheet resistance [5,6].

The aim is to reduce the Indium consumption through different basic strategies that can be classified into three main paths. The first route is the development of Indium-free Transparent Electrodes (TE), such as Al-doped Zn oxides (AZO) or AZO/Ag/AZO multilayer structures [7–11], conductive Polymers as PEDOT PSS [12], metallic nanowires meshes, grids [13–16], and carbon nanotubes [6].

The second possibility moves toward the recycling of Indium from decommissioned solar cells or sputtering deposition waste (from ITO

* Corresponding author. AMOLF Physics of Functional Matter, Science Park 104, NL1098XG, Amsterdam, the Netherlands.
E-mail address: M.Micali@amolf.nl (M. Micali).

https://doi.org/10.1016/j.solmat.2024.112875
Received 25 January 2024; Received in revised form 19 March 2024; Accepted 12 April 2024
Available online 20 April 2024

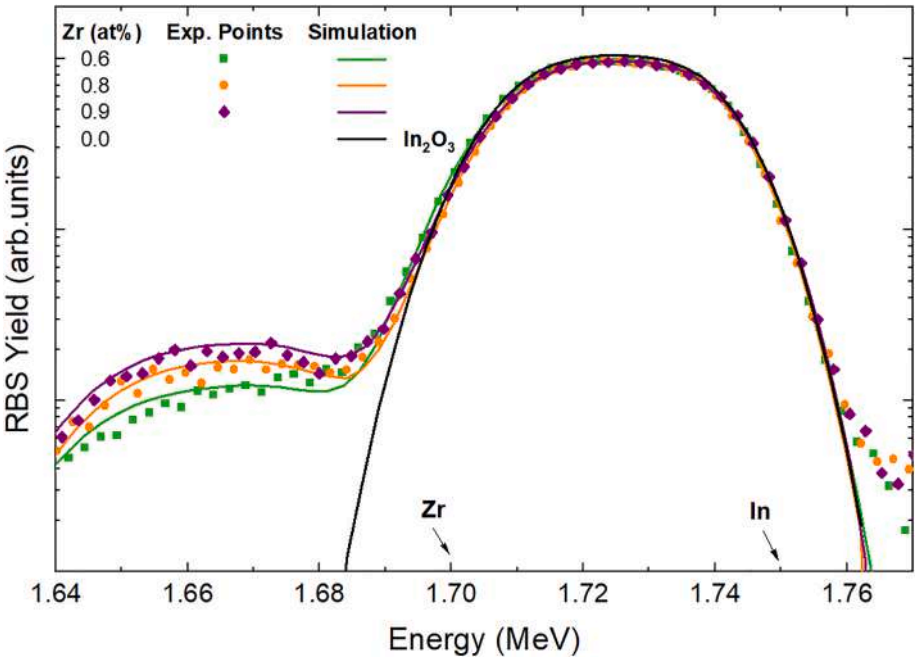

Fig. 1. RBS experimental spectra (dots) and simulated curves with SimnNra software (lines) for different as-deposited IZrO samples, in a semi-log scale. Data are relative to 40 nm films, with different Zr concentration of 0.6 at.%, 0.8 at.% and 0.9 at.%. Black arrows in the graph indicate the theoretical backscattering energies for Zr and In at the surface.

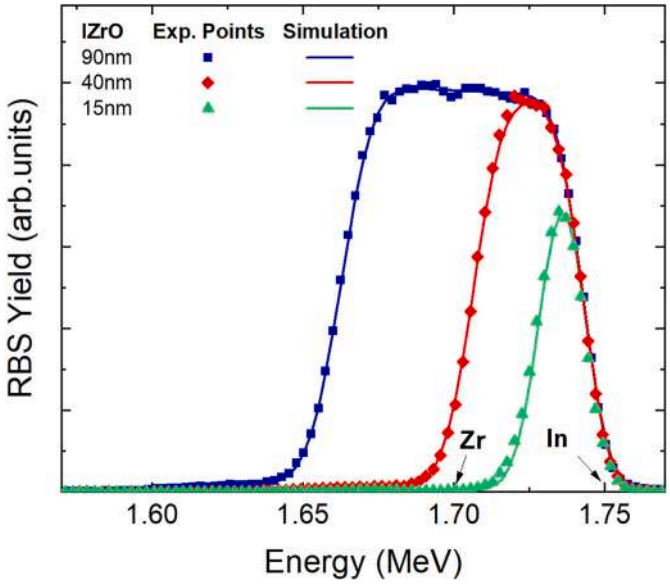

Fig. 2. RBS experimental spectra (dots) and simulated curves with SimnNra software (lines) for as-deposited IZrO samples with 0.6 at.% of Zr and different thicknesses. Black arrows in the graph indicate the theoretical backscattering energies for Zr and In at the surface.

Table 1
Elemental concentrations of the three as deposited 40 nm thick films.

Zr [at.%]	In [at.%]	O [at.%]
0.6	38.8	60.6
0.8	35.8	63.4
0.9	35.8	63.3

Table 2
Thickness and elemental concentrations of three as deposited films with fixed Zr = 0.6 at.%.

Thickness [nm]	Zr [at.%]	In [at.%]	O [at.%]
90	0.6	36.8	62.6
40	0.6	38.8	60.6
15	0.6	38.8	60.6

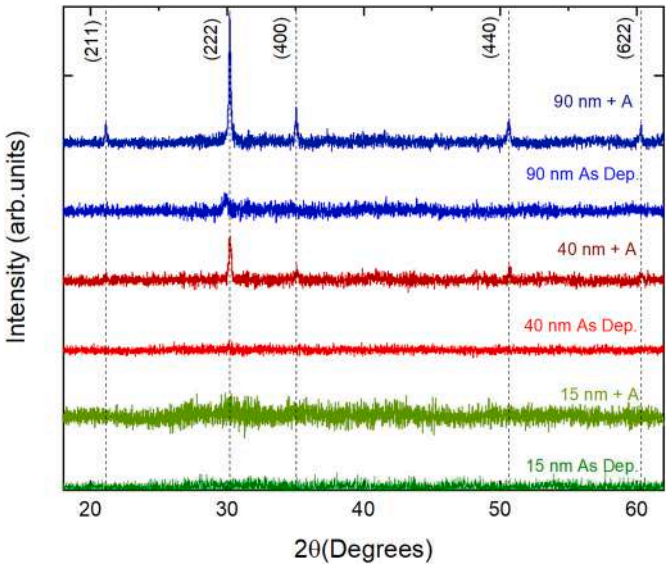

Fig. 3. XRD diffractograms for as-deposited and annealed (T = 200 °C in air) IZrO films with different thicknesses.

deposited on the equipment or unused targets). The third approach is a consistent reduction of the use of indium by decreasing the thickness of the TCO films. The latter has also the advantage of being easily implemented in the industrial processes. In this work, we focused on the third

Table 3
(hkl) Miller indexes, 2θ angles, relative intensities of the peaks, and the average grain size of our polycrystalline IZrO films before (As Dep.) and after the annealing (+A).

Sample Name	*hkl*	**2θ [Degrees]**	**Relative Intensity [%]**	**Average grain size [nm]**
IZrO 90 nm As Dep.	222	29.90	100	20.52
IZrO 90 nm + A	211	21.12	16.24	
-	222	30.20	100	42.04
-	400	35.06	28.98	
-	440	50.64	17.87	
-	622d	60.32	15.17	
IZrO 40 nm + A	222	30.23	100	30.53
-	400	35.12	39.36	
-	440	50.70	38.68	

solution by reducing TCO thickness from the standard value of about 100 nm, commonly used in the industrial Si-based solar cells, down to 15–20 nm. Although such a thin TCO could modify the light reflection at the cell surface, this effect can be solved by optimizing the anti-reflective coating film [17,18].

The main issue for a TCO with reduced thickness is related to the consequent sheet resistance increase. Thus, the key point is the doping of Indium Oxide with impurities which can improve the conductivity more efficiently as compared to Sn in ITO.

In ITO, the strong hybridization between In and Sn *5s* orbitals at the bottom of the conduction band of In_2O_3 can enlarge the band curvature. In fact, the reciprocal of the effective mass in the dispersion relation is proportional to the curvature of the band, so that the smaller the effective mass value, the sharper the curvature of the band. To this purpose, Transition Metals (TM) have been proposed as promising dopants for In_2O_3. When a TM is introduced as a dopant, the hybridization between the TM *d* levels and In *5s* states is weak and the band curvature around the conduction band minimum is maintained, leading to an electron effective mass lower than ITO, with a consequent higher carrier mobility. In terms of their ground-state electronic structures, TM dopants can be generally classified into three types. For Type-I donors, n-type doping cannot be achieved at room temperature (Ti, V, Cr, and Mo) because the defect levels are significantly lower in energy than the conduction band maximum (CBM) of In_2O_3. For Type-II donors (Nb and W) the defect levels are above the CBM of In_2O_3, but since they are not high enough in energy, the carrier density n_e will be limited. For Type-III donors (Zr, Hf, and Ta), the defect levels are sufficiently high in energy above the CBM of In_2O_3, so that TM dopants can be fully ionized, acting as shallow donors, and the electron effective mass m_e can be largely maintained; therefore, ideal n-type doping could be realized with high carrier mobility μ_e and concentration n_e [19].

In this work, we report the growth and characterization of Zr-doped In_2O_3 (IZrO) thin films. As reported in the literature, these films are mainly grown by magnetron sputtering [20–24], with a low Zr concentration (Zr = 2 wt%), showing very promising opto-electrical performances.

In our case, a preliminary study has been carried out with different Zr at.% to evaluate the best donor concentration for the highest mobility and optical transmittance. Then, keeping the Zr at.% fixed, the optical and electrical properties were studied as a function of the thickness, from the standard values of about 100 nm used in crystalline Si solar cells down to 15 nm. Ultra-thin films were deposited at room temperature, followed by post-deposition thermal treatment at T = 200 °C in air, to make the synthesis procedure compatible with industrial fabrication processes and applications in flexible devices with polymer substrates.

Table 4
Root Mean Square roughness (RMS) of IZrO films with different thicknesses before (as-deposited) and after annealing. All the samples have been deposited with a fixed Zr = 0.6 at.%.

IZrO film thickness [nm]	**RMS of as-deposited films [nm]**	**RMS of annealed films [nm]**
15	1.17	0.85
40	0.88	1.21
90	1.76	2.11

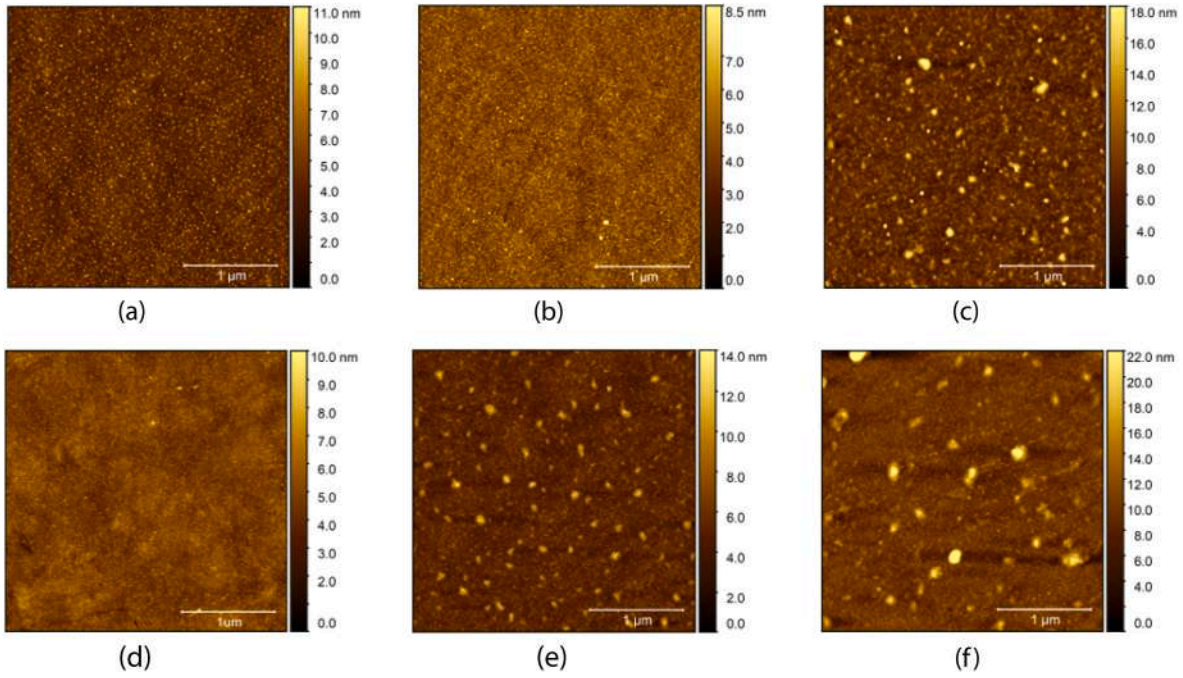

Fig. 4. AFM scans (3 µm × 3 µm) of Zr = 0.6 at.% IZrO films, as-deposited (a, b, c) and annealed (d, e, f) for different thicknesses: 15 nm (a, d), 40 nm (b, e), 90 nm (c, f).

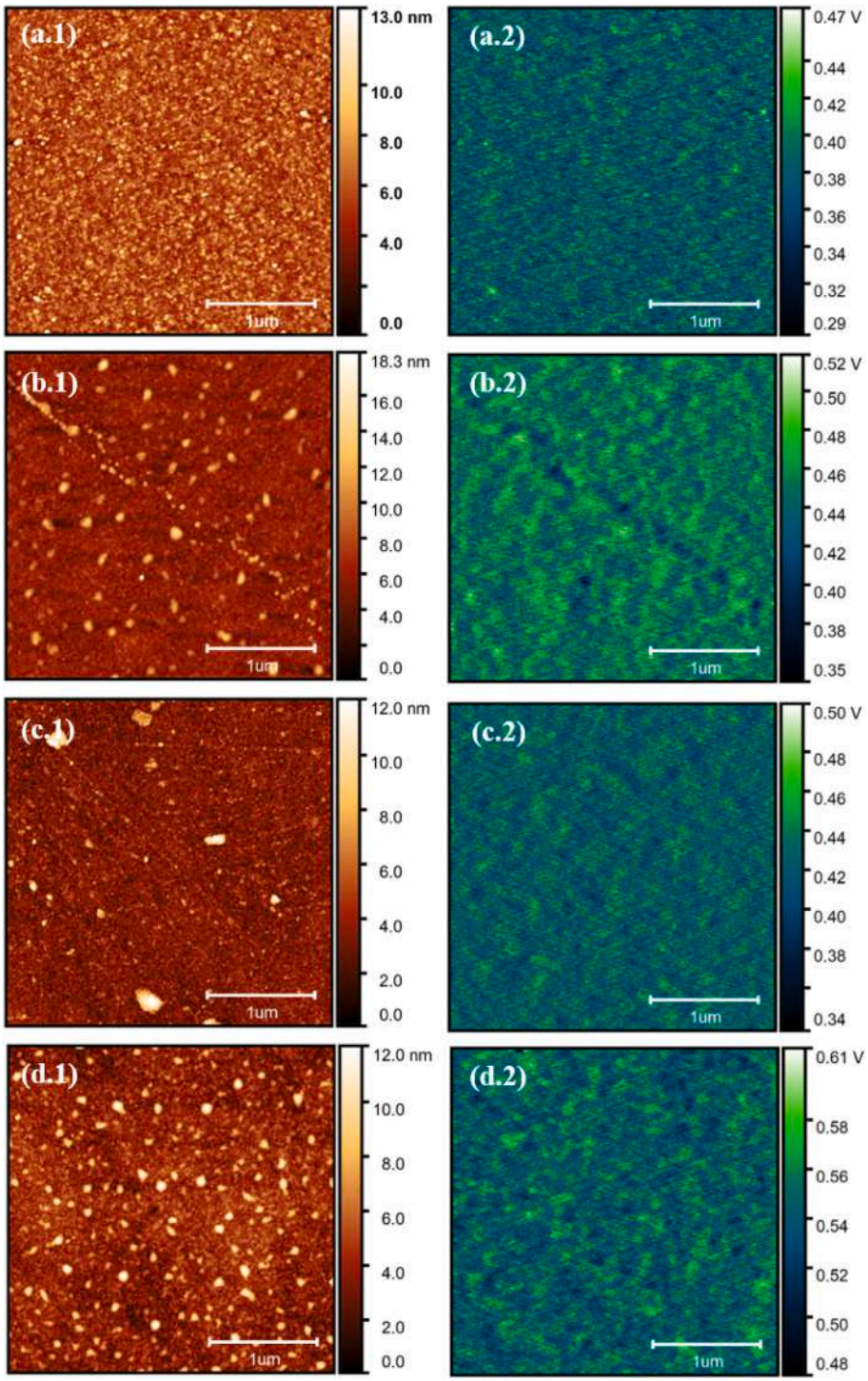

Fig. 5. Surface morphology and surface potential maps from FM-KPFM measurements for IZrO films with different Zr at.%: 0 (a.1-a.2), 0.6 (b.1- b.2), 0.8 (c.1-c.2), 0.9 (d.1- d.2). All the samples are 40 nm thick.

Table 5
Work Function and Root Mean Square (RMS) in eV for IZrO 40 nm thick films, with different Zr at.%.

Zr [at.%]	W_F [eV]	RMS [eV]
0	4.51	0.02
0.6	4.57	0.02
0.8	4.55	0.02
0.9	4.65	0.02

2. Experimental section

Deposition of IZrO thin films: Zirconium doped Indium Oxide thin films (IZrO) were deposited on high purity quartz glass materials (>99,95 % - Spi supplies) and Si p-type substrates by RF and DC Magnetron co-sputtering technique from In_2O_3 and Zr target (2-inch diameter) supplied by Moorfield Nanotechnology with 99,99 % purity. Depositions were performed at room temperature in a pure Argon atmosphere with a gas flow of 6 sccm and a working pressure of 1.6×10^{-2} mbar. A sputtering power of 45 W was used for In_2O_3 in RF mode

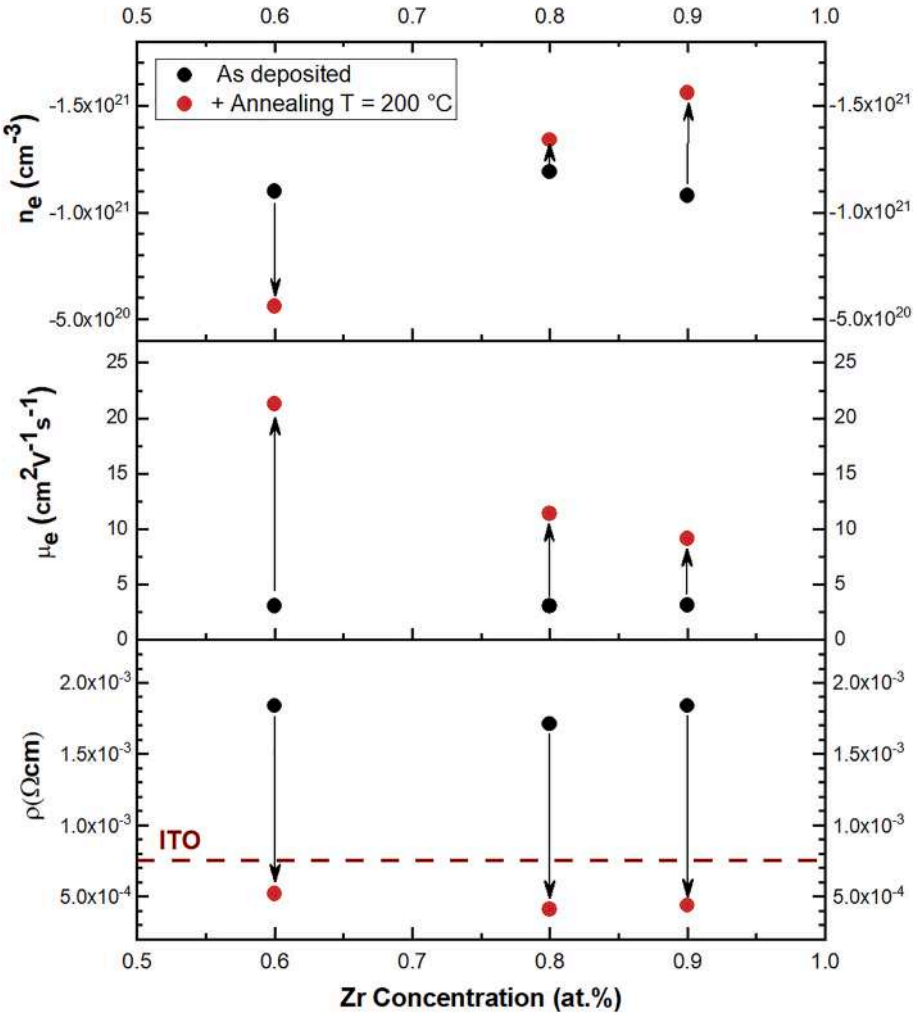

Fig. 6. Resistivity ρ, Mobility μ_e and Carrier Concentration n_e behavior of IZrO films with different Zr at.%: 0.6 at.%, 0.8 at.% and 0.9 at.% with a fixed thickness of 40 nm, before (black squares) and after (red squares) post-deposition thermal annealing.

and 57 W for Zr in DC mode. The sputtering system was used in a sputter-up configuration with a rotating sample holder to guarantee uniform thickness distribution and composition in a 4 × 4 cm^2 area. Two different sets of three samples were grown: the first set with different Zr at.% concentration and the second one with different thickness (i.e. longer depositions).

Previous tests made clear that the DC power supply yields sputtering rates comparable to those of the RF one, even at lowest DC power; therefore, without any action, the resulting samples would be an Indium Oxide – Zirconium alloy rather than a Zr-doped oxide. To strongly decrease the Zr deposition rate, we installed a cover with an adjustable slit width just above the DC biased Zr target, so limiting and controlling the Zr deposition rate. The slit widths for different Zr at.% were adjusted and measured with a gauge, and the apertures were set to be 0.8, 1.0 and 1.2 mm wide. Post-deposition thermal annealing was performed at 200 °C for 30 min in air atmosphere.

RBS Measurements: Rutherford backscattering spectrometry (RBS) was employed to quantify the doses of chemical elements in the films and to convert them into thickness dividing by the atomic density of the material. RBS measurements were performed using a Singletron ion accelerator with a 2.0 MeV He^+ ion beam at normal incidence with the backscattered ions detected at an angle of 165°. SimNra software was used to simulate the experimental RBS spectra collected for the quantitative analysis.

XRD Measurements: Bruker Diffractometer 2D Phaser was used for X-Ray Diffraction measurements. The tool was operated at 30 kV, 10 mA, at 2θ (Cu $K_{\alpha1} = 0.15406$ nm, Cu $K_{\alpha2} = 0.15444$ nm) from 10° to 80° at step = 0.010°.

AFM Measurements: Bruker Dimension Icon Atomic Force Microscopy was used for AFM measurements in a Peak Force Tapping Mode using a Silicon Nitride probe provided by Bruker (ScanAsyst-Air).

FM-KPFM Measurements: Bruker Dimension Icon Atomic Force Microscopy has been used in Peak-Force Tapping mode for Frequency Modulated Kelvin Probe Force Microscopy measurements (FM-KPFM) to measure the work function of the samples. A PFQNE-AL heavily doped silicon probe, calibrated with a reference Au sample, was used to collect surface potential maps.

Electrical Characterization: Sheet resistance R_{sh}, Hall mobility μ_e, and carrier concentration n_e were measured by 4-point probe in the Van der Pauw configuration at room temperature with a Hall Effect Measurements System HL5500PC.

Optical Characterization: Varian Cary 500 double beam scanning UV-VIS-NIR spectrophotometer was used to measure the direct optical transmittance (T) and specular reflectance (R) in the 250–2500 nm wavelength range. Transmittance (T) spectra in normal incidence were collected with a 100 % baseline obtained without sample, while the reflectance (R) spectra have been detected in specular geometry at 20° using a calibrated standard. Tauc analyses were performed to determine the energy gap of the samples.

SEM Analysis: The surface samples morphology of textured SHJ solar cells with IZrO deposited as transparent electrodes, was investigated by field emission scanning electron microscopy (SEM) using a Zeiss Supra

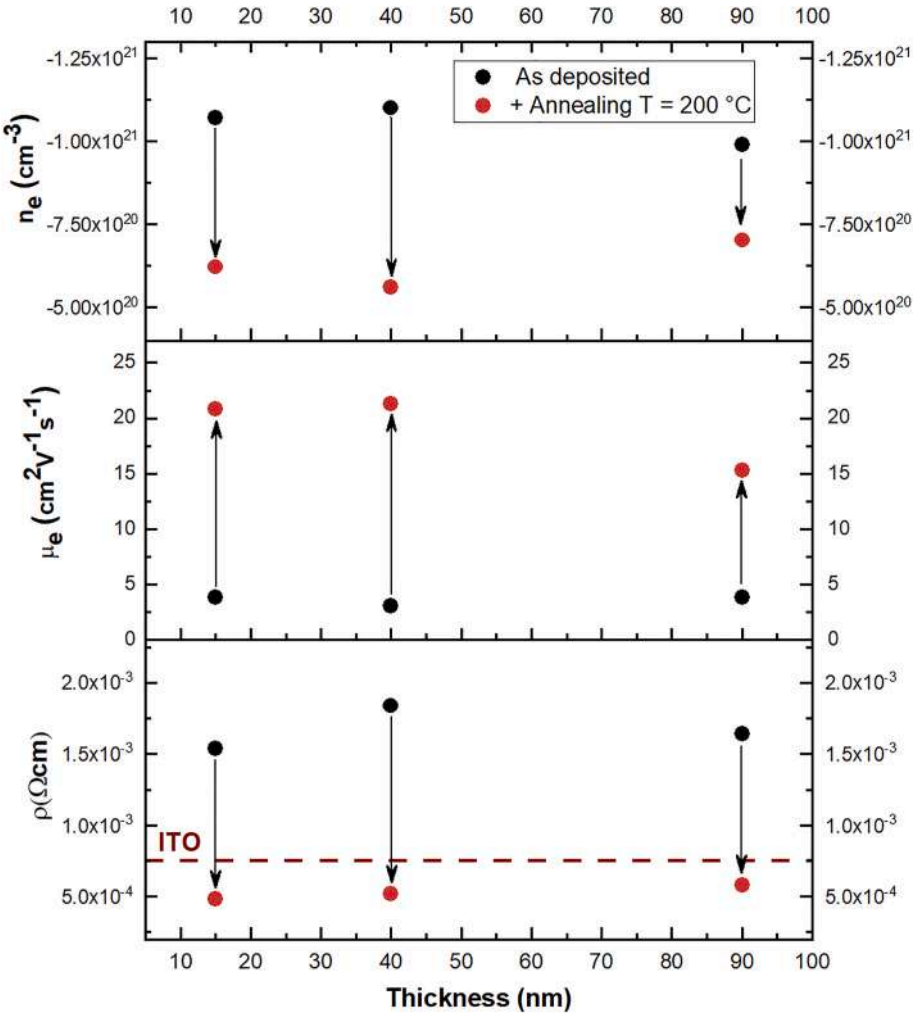

Fig. 7. Resistivity ρ, Mobility μ_e and Carrier Concentration n_e behavior of IZrO films with different thickness 15 nm, 40 nm and 90 nm at fixed Zr concentration of 0.6 at.%, before (black squares) and after (red squares) post-deposition thermal annealing.

Table 6
Sheet Resistance values comparison reported for different ultra-thin TCO: IZrO films of 15 nm thickness from this work compared with ITO and AZO of 20 nm thickness from the literature.

Sample Name and thickness [nm]	R_{sh} [Ω/□]
IZrO 15 nm [this work]	344
ITO 20 nm [26]	623
AZO 20 nm [26]	876

25 microscope operating at 1.0 kV in InLens operation mode.

External Quantum Efficiency (EQE): The external quantum efficiency curves of samples were acquired through Bentham PV300 photovoltaic QE system. The experimental setup used for the EQE measurements consists of a monochromator, a thermostatic golden plated chuck, as a potential reference, a c-Si reference PV cell used for the calibration of the EQE detection system, a lock-in controller for modulating the light source's power and an electrical current measure unit. The samples, of square shape, were connected to the electrical current measure unit by a conductive tip and held in a fixed position by vacuum suction near the light spot (3 × 3 mm) to achieve the maximum current extraction. The samples' detector responsivity was acquired from 300 to 1100 nm with a step of 5 nm. The extracted current for each wavelength with its specific radiation power represents the detector responsivity (DR) of the sample. The DR is reported in A $W^{-1}nm^{-1}$ and the EQE trends of the solar cell

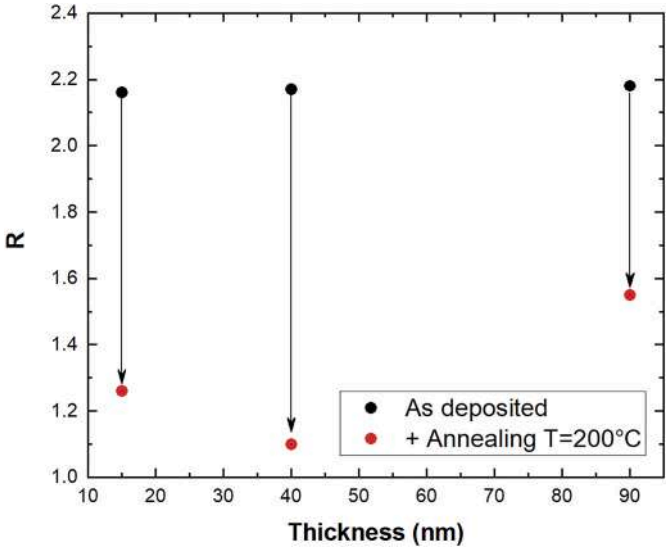

Fig. 8. Activation Rate for films with different thickness of 15 nm, 40 nm, and 90 nm and fixed Zr = 0.6 at.%, as-deposited (black squares) and after (red dots) post-deposition thermal annealing at T = 200 °C.

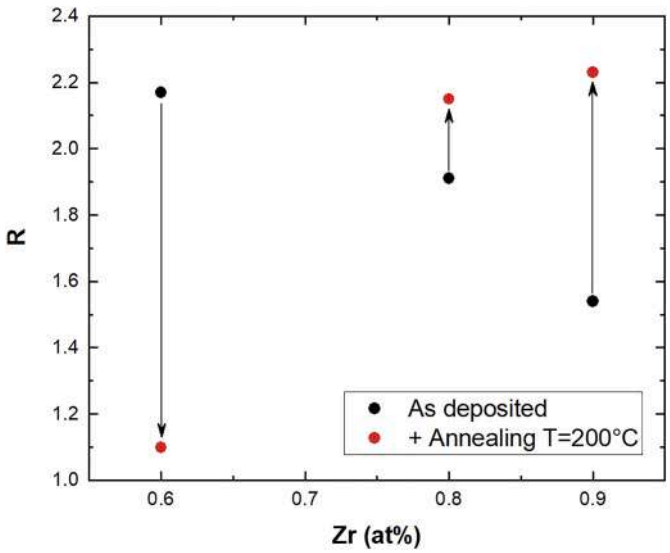

Fig. 9. Activation Rate for films with different Zr at.% of 0.6 at.%, 0.8 at.% and 0.9 at.% and fixed thickness of 40 nm, before (black squares) and after (red dots) post-deposition thermal annealing.

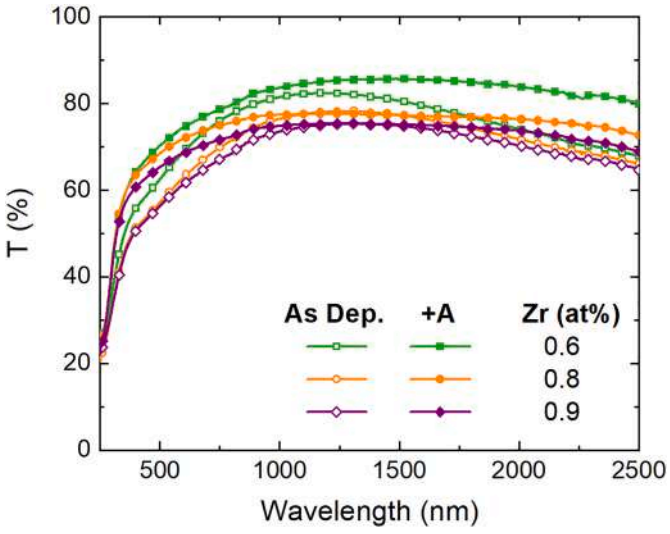

Fig. 10. Transmittance spectra for IZrO films with different Zr at.% of 0.6 at.%, 0.8 at.% and 0.9 at.% and a fixed thickness of 40 nm, before (As Dep.) and after (+A) post-deposition thermal annealing at T = 200 °C.

samples are obtained from the DR by converting the radiation power into number of photons.

Semifinite solar cells fabrication: The cells were fabricated starting from Cz n-type silicon wafers and processed in the fully automated 3SUN solar cell production line. Firstly, the wafers are homogeneously texturized in an alkaline solution and an addition of texturization additives. Acids baths are used to eliminate the metallic impurities present on the surface of the wafers and to eliminate native SiO_2 before the deposition of amorphous silicon layers. Intrinsic a:Si layers are deposited on both the back and front side of the cell in a Meyer Burger PECVD tool. The cells are finally capped with p doped amorphous silicon layer on the back and n doped amorphous silicon layer on the front. The semifinite cells are finally completed depositing either IZrO or ITO layers. The ITO layers are obtained in a Meyer Burger industrial Sputtering tool in DC pulsed mode introducing Ar and O_2 in the reaction chamber. Both layers of the cell are completed depositing around 100 nm of ITO.

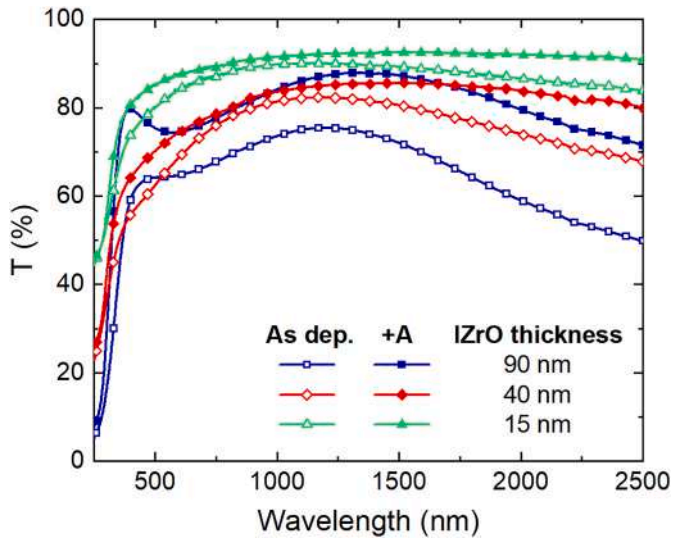

Fig. 11. Transmittance spectra for IZrO films with different thickness of 90 nm, 40 nm, and 15 nm and a fixed Zr = 0.6 at.%, before (As Dep.) and after (+A) post-deposition thermal annealing at T = 200 °C.

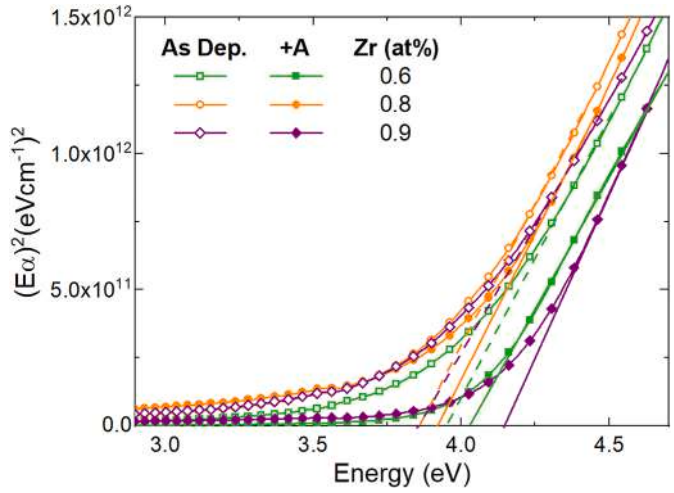

Fig. 12. Tauc Plot for IZrO films with different Zr at.% of 0.6 at.%, 0.8 at.% and 0.9 at.% with a fixed thickness of 40 nm, before (As Dep.) and after (+A) post-deposition thermal annealing.

3. Results and discussion

3.1. RBS measurements

Structural analyses were done via Rutherford Backscattering Spectrometry (RBS). RBS spectra of as-deposited IZrO thin films with different Zr content are shown in Fig. 1. The simulated spectrum of a pure In_2O_3 film is reported for comparison. Data are reported in a semi-log scale of the RBS yield vs. the energy of the backscattered He^+ ions in the region of interest for Zr and In. The semi-log scale in the chosen region allows to clearly resolve the small amount of Zr present in the films. The experimental spectra (dots in Fig. 1) were simulated by SimNra software for quantitative analysis (solid lines). The arrows indicate the energies of ions backscattered by Zr and In at the surface, while the RBS peak areas are proportional to the atomic density of the element integrated over the thickness of the film.

The deposition time for this first set of samples was fixed to obtain the same thickness, estimated at 40 nm using the atomic areal density (atoms/cm^2) simulated with the software and the atomic density of the

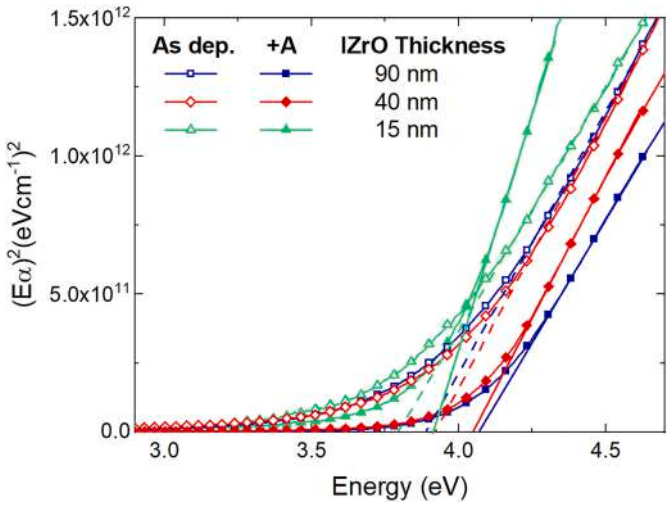

Fig. 13. Tauc Plot for IZrO thin films with different thickness of 15 nm, 40 nm, and 90 nm with a fixed Zr = 0.6 at.%, before (As Dep.) and after (+A) post-deposition thermal annealing.

Table 7
Mean Values of transmittance in the VIS range ($<T>_{VIS}$) and NIR range ($<T>_{NIR}$) and energy gap values (E_g) for different Zr at.% of 0.6 at.%, 0.8 at.% and 0.9 at.% with a fixed thickness of 40 nm, before (As Dep.) and after (+A) post-deposition thermal annealing.

Sample Name	$<T>_{vis\ (380\text{-}780)}$ [%]	$<T>_{NIR\ (780\text{-}1500)}$ [%]	E_g [eV]
Zr = 0.6 at% As Dep.	60.2	81.15	3.95
Zr = 0.6 at% + Annealing	72.3	84.06	4.04
Zr = 0.8 at% As Dep.	60.62	76.59	3.86
Zr = 0.8 at% + Annealing	70.06	77.2	3.92
Zr = 0.9 at% As Dep.	59.17	73.76	3.85
Zr = 0.9 at% + Annealing	66.86	74.78	4.12

material (d_{IZrO} = 7.69 × 10^{22} at/cm^3). The analysis of RBS spectra pointed out a Zr content ranging from 0.6 at.% to 0.9 at.%.

In Fig. 2, the RBS spectra of a second set of samples with a fixed Zr concentration of 0.6 at.% are reported in linear scale. The peak areas and widths are proportional to the film thickness, resulting in three different values of 90, 40 and 15 nm.

The RBS graphs over the entire range are reported in Fig. S1 and Fig. S2 of the Supporting Information (SI). The fit of RBS data in Figs. 1 and 2 provided us the quantitative values listed in Table 1 and Table 2.

Table 8
Mean Values for transmittance in the VIS range ($<T>_{VIS}$) and NIR range ($<T>_{NIR}$), and Energy gap values (E_g) for d for different IZrO film thickness of 90 nm, 40 nm and 15 nm with a fixed Zr = 0.6 at.%, before and after post-deposition thermal annealing.

Sample Name	$<T>_{vis\ (380\text{-}780)}$ [%]	$<T>_{NIR\ (780\text{-}1500)}$ [%]	E_g [eV]
90 nm As Dep.	64.27	73.49	3.89
90 nm + Annealing	76.18	85.3	4.07
40 nm As Dep.	66.26	81.15	3.92
40 nm + Annealing	72.35	84.08	4.05
15 nm As Dep.	82.27	89.60	3.77
15 nm + Annealing	86.11	91.78	3.91

3.2. XRD measurements

Pristine crystalline In_2O_3 films are characterized by the presence of diffraction peaks along (211), (222), (400), (440) and (622) planes of the unit cubic bixbyite structure [24]. Fig. 3 shows the X-Ray Diffractograms of as-deposited and annealed (T = 200 °C) IZrO samples for different thicknesses.

The as-deposited films exhibit an amorphous structure for the 15 and 40 nm samples, while a weak (222) diffraction peak is visible for a thickness of 90 nm. This result is in agreement with the literature reporting the crystallinity enhancement with thickness of room temperature sputter-deposited TCO [25]. As for the annealed samples, they show a clear transition to the crystalline phase, except for the thinnest one (15 nm) which is probably below the minimum thickness for the sensitivity of the used equipment.

The 2θ positions of the detected peaks, assigned crystallographic planes and relative intensities are listed in Table 3. If compared to the reference, some peaks are slightly shifted towards higher angles and this can be attributed to the presence of Zr interstitial atoms inducing lattice strain. The relative intensities of the peaks confirm the preferred orientation towards the (222) plane according to the In_2O_3 bixbyite structure.

Additional information can be obtained via analysis of the peaks width. In fact, the Full-Width Half Maximum (FWHM) is related to the average size *D* of the single crystalline domain within the polycrystalline films according to the Scherrer Formula (equation 1):

$$D = \frac{K\lambda}{W cos\theta} \quad (1)$$

where K = 0.9 is the Scherrer constant, λ is the XRD wavelength, $\theta = 2\theta/2$ is the peak position and W is the FWHM of the peak.

XRD patterns for the (222) peak of crystalline samples (IZrO 90 nm as-deposited, 40 nm + A, 90 nm + A) were collected at high resolution and subsequently fitted with Gaussian function to extrapolate the FWHM of the peaks. The FWHM were corrected considering the instrumental broadening, which was previously estimated from a Corundum sample used as a reference. We calculated an average crystal size *D* for IZrO films of 20.52 nm for 90 nm as-deposited films, and 30.53 nm and 42.04 nm for annealed films of 40 nm and 90 nm respectively. A reduction of the FWHM and the corresponding increase of *D* is related to an improvement of the crystalline quality of the film as confirmed by the XRD spectra. The related Fig. s with Gaussian peaks fit are reported in SI (Fig. S3, Fig. S4, Fig. S5, and Table S1).

3.3. AFM measurements

The surface morphology of IZrO films with different thicknesses was investigated by atomic force microscopy (AFM) as shown in Fig. 4. All the films exhibit a smooth surface, with surface roughness values around 1–2 nm, as listed in Table 4 in terms of Root Mean Square (RMS). For the as-deposited samples, the increase of the thickness leads to the formation of larger grains, that further aggregate in clusters upon annealing.

3.4. FM-KPFM measurements

The Work Function (WF) of IZrO thin films as a function of the doping concentration was extracted through surface potential mapping with Frequency Modulated – Kelvin Probe Force Microscopy (FM-KPFM) measurements. The morphology and the complementary surface potential maps of 3 μm × 3 μm scan-size for the three different Zr atomic concentrations (0.6 at.%, 0.8 at.%, and 0.9 at.%) after annealing are shown in Fig. 5 and compared with pure In_2O_3 to study the effect of Zr doping on the WF. A heavily doped Silicon probe (PFQNE-AL) was calibrated using a Au reference sample (Φ_{Au} = 5.01 *eV*), according to the relation $\Phi_{Tip} = \Phi_{Au} - eV_{CPD}$. For every map, the average value of the

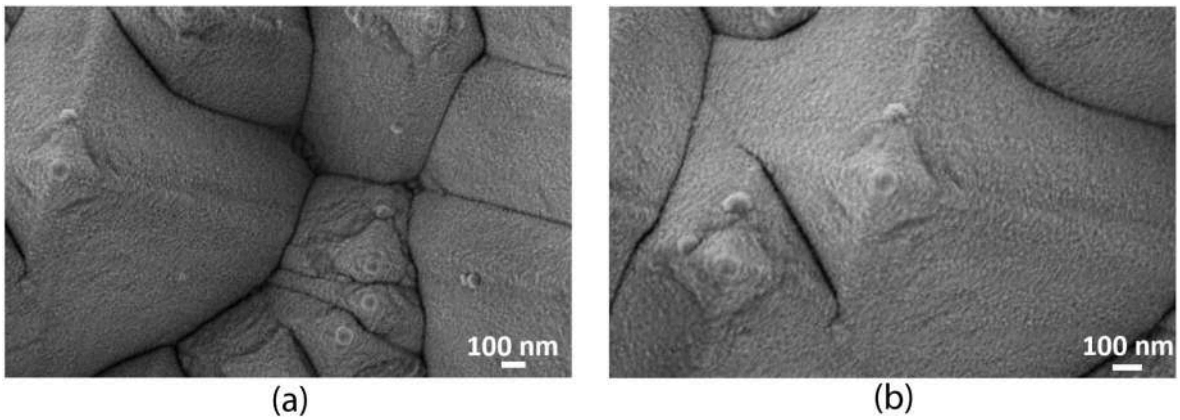

Fig. 14. Top view SEM images of 90 nm IZrO deposited on top of bifacial SHJ solar cell.

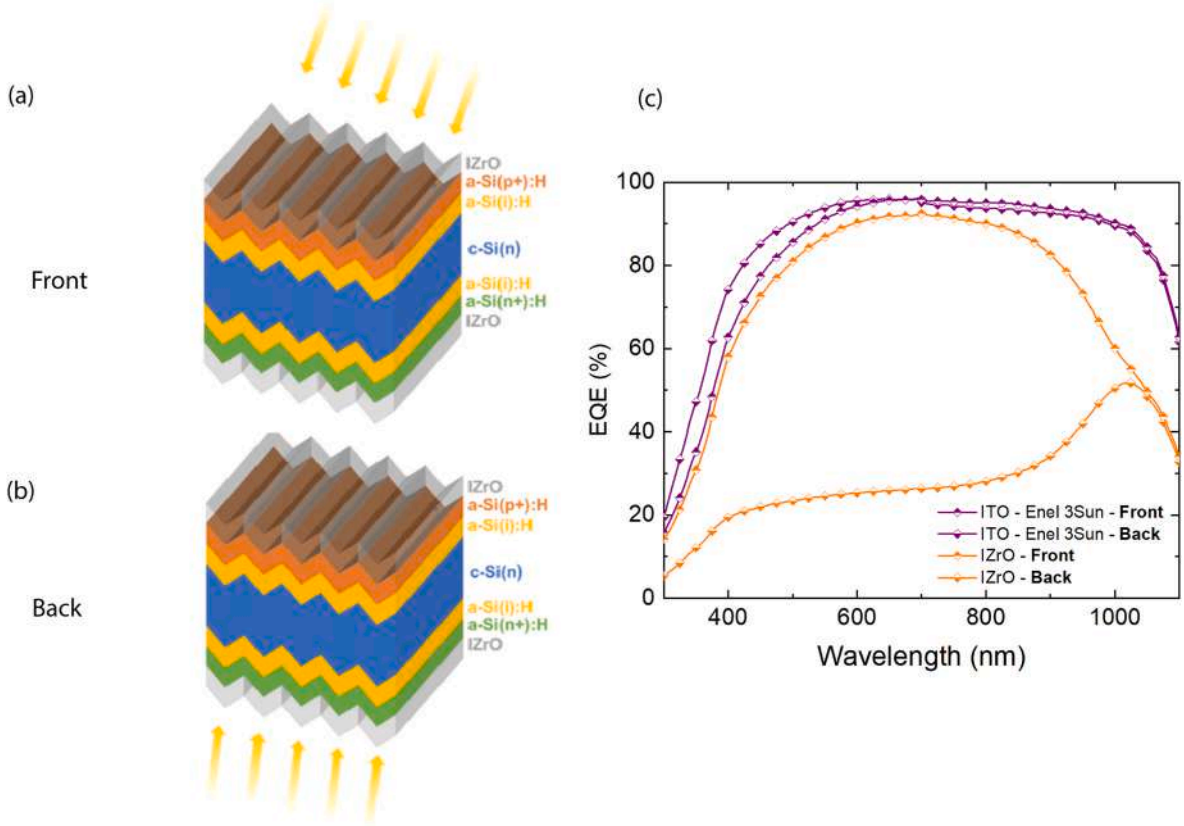

Fig. 15. EQE data obtained from measurements on bifacial SHJ solar cell with 90 nm of IZrO deposited as TE after thermal annealing at T = 200 °C. The data have been obtained with two different configuration: a) shining light onto the IZrO/a-Si(p+):H side and b) shining light onto the IZrO/a-Si(n+):H side; c) EQE values for SHJ solar cell with IZrO electrodes (orange curves) deposited as front and back contacts compared with EQE on SHJ solar cell with ITO as electrodes (purple curves) deposited by Enel 3SUN as front and back contact. Both samples were investigated in "front" and "back" experiment configurations.

surface potential was extracted by further analysis, and the WF is calculated according to the relevant equation for the Tip biasing mode:

$$\Phi_{Sample} = \Phi_{Tip} + eV_{CPD} \quad (2)$$

The WF values obtained are listed in Table 5. A clear effect of the Zr introduction is the increase of the WF from 4.51 eV up to 4.65 eV. The maps also highlight a nearly uniform WF over the whole scanned area.

3.5. Electrical properties

The electrical characterization was performed with a four-point probe in Van Der Pauw configuration within a Hall system, to measure the Sheet Resistance R_{sh}, the carrier mobility μ_e and concentration n_e. From the R_{sh} and film thickness, the resistivity ρ was calculated. All the values are reported in Tables S2 and S3 in the SI. For both sets of samples, the thermal annealing clearly improves the electrical properties with a decrease in the resistivity and higher values of carrier mobility, despite a decrease of the carrier concentration. Fig. 6 shows the electrical resistivity for samples with different Zr at.% and thickness fixed at 40 nm, before and after the post-deposition thermal annealing, compared with standard ITO [26]. The trend shows a decrease in the electrical resistivity from 10^{-3} Ωcm down to $4 \bullet 10^{-4}$ Ωcm, with lower values compared to ITO ($7 \bullet 10^{-4}$ Ωcm). The data point out that for the lowest dopant content ($Zr = 0.6$ *at.*%) the films have the best electrical

properties, with the highest carrier mobility of 21 $cm^2V^{-1}s^{-1}$ and the lowest carrier concentration $5.4 \bullet 10^{20}$ cm^{-3}.

Fig. 7 reports the electrical properties of IZrO films with fixed dopant concentration ($Zr = 0.6$ *at.*%) and varying thickness. To compare the electrical performance for different materials with the same thickness, we listed the Sheet Resistance of ultra-thin TCO films in Table 6: ITO 20 nm [26] and AZO 20 nm [27] from literature, compared to our IZrO 15 nm. The data show promising results, as $R_{sh} = 344\ \Omega/\square$ for IZrO compares to 623 $\Omega/\square$ and 876 $\Omega/\square$ for ITO and AZO respectively.

In addition, the activation Rate (R) for the Zr donors was estimated as the ratio between the carrier density (from Hall measurements) and the dopant concentration (from RBS analysis), assuming that every Zr atom in a substitutional Indium site contributes with one electron in the conduction band:

$$R = \frac{Measured\ Carrier\ Density}{Measured\ Zr\ Concentration} \tag{3}$$

Carrier concentrations are listed in Table S4 and Table S5 in the SI. The activation Rate for samples with Zr atomic concentration of 0.6 at.% (Fig. 8) and fixed thickness of 40 nm (Fig. 9), are compared before and after post-deposition thermal annealing. The general trend always shows R values higher than 1, so indicating that Zr is not the only dopant in our IZrO films. In fact sputter deposited In_2O_3 is known [1] to exhibit an n-type intrinsic doping mechanism due to the oxygen vacancies that contribute to the carrier density providing 2 electrons per vacancy. Despite the expected enhancement of the doping efficiency upon thermal annealing due to promotion of Zr into substitutional sites, we observe a strong decrease of R in several cases. This phenomenon, reported for all samples of Fig. 8, can be attributed to the diffusion of oxygen from the annealing atmosphere into the IZrO films, partially compensating oxygen vacancies which can be the dominant doping source in samples with the lowest Zr content (0.6 at.%).

This behavior is reversed in samples with higher Zr concentration (Fig. 9), for which the contribution of the extrinsic doping (Zr donors) increases as compared to the intrinsic one (Oxygen vacancies).

3.6. Optical properties

Fig. 10 and Fig. 11 show the transmittance spectra for samples with different Zr at.% (fixed thickness) and with different thicknesses (fixed Zr at.%) respectively, both before and after the thermal treatments. The effect of post-deposition thermal annealing is the improvement of the optical properties for all sets of samples, increasing the mean values of the transmittance (<T>) in the full range. This can be related to an enhanced crystalline quality of the films, as suggested by the XRD measurements shown in Section 2.2. From Fig. 10, a degradation of the transmittance is observed when the Zr concentration increases. Moreover, the thermal annealing improves the optical properties in all samples.

As expected, Fig. 11 points out that decreasing the thickness of the films results in an improved optical transmittance over the whole range. It is also worth noting that the reduction of free carriers upon annealing reflects in a weaker plasmonic absorption in the NIR region. The reflectance spectra for both sets of samples are reported in Fig. S6 and Fig. S7 in the SI.

The optical band gap was calculated using the following Tauc's equation [28] for direct transitions:

$$(E\alpha)^2 = B(E - E_{gap}) \tag{5}$$

where B is the Tauc coefficient, α the absorption coefficient, and E the photon energy. In this way, E_{gap} is obtained from x axis intercept of the linear fit of the linear portion of the Tauc plots, as shown in Fig. 12 and Fig. 13 for different Zr at.% and different thicknesses, respectively.

For all the samples, α was calculated by using the following equation [29].

$$\alpha = \frac{1}{d} In \frac{T_G(1 - R_s)}{T_s} \tag{6}$$

where d, T_s, and R_s are the thickness, transmittance, and reflectance of the sample respectively, while T_G is the transmittance of the glass substrate. The band-gap values are close to 3.91 eV before annealing with a slight increase up to 4.12 eV after the thermal treatment, confirming the nature of wide band gap TCO for IZrO. The energy gap and mean values of transmittance are listed in Table 7 and Table 8.

3.7. Device characterization

To test the performances of a proof-of-concept solar cell based on IZrO electrodes, we deposited IZrO films on bi-facial Silicon Heterojunction solar cells, extracted from the production line right before the deposition of the transparent electrode layers. The incomplete cell was fabricated by the 3SUN company with the structure of a-Si(p+):H/a-Si(i):H/c-Si(n)/a-Si(i):H/a-Si(n+):H, taken out of the production line and transported to the university laboratory for the two-steps deposition of 90 nm IZrO films, both as front and back contact. The cells were then annealed at T = 200 °C in air atmosphere. As a reference, the commercial cell by 3SUN Company, with ITO as front and back electrode, was tested. Fig. 14a and b shows plan view SEM micrographs at different magnifications after the deposition of IZrO films, proving that the textured morphology of the cell is excellently preserved.

Fig. 15c shows the EQE measurements for both cells with IZrO electrodes (orange curves) and ITO electrodes (purple curves). The EQE was measured shining light either from the front (Fig. 15a) or from the back (Fig. 15b) of the device.

When light is shone onto the p-side of the IZrO based cell ("front" configuration), EQE values are satisfyingly comparable to the ITO based one over the UV and Visible wavelength range. On the other hand, the device performance is degraded for wavelengths above ≈850 nm, most probably because the film thickness is not optimized to effectively work as anti reflective layer.

The performance of the device, when light is shone on the n-side of the cell, is not good. The EQE curve presents high losses from UV to NIR range, of about 50 % in relation to the reference cell; it is reasonable to attribute this drop to a poor electrical coupling between the electrode and the cell. A first consideration comes from the different work function of a-Si(n+):H, of about 4.1–4.2 eV [30], and of IZrO, as high as ≈4.6 eV, as measured via KPFM in this work. Such WF mismatch forces a high band bending at the interface, limiting the charge collection efficiency and also depleting the a-Si(n+):H layer because of the very high charge density in TCO. Plus, the two-steps deposition of IZrO films (on p-side and then on n-side) might have been detrimental for the overall device integrity, leading to performance loss that we cannot quantify reasonably. In addition to the electrical losses, the EQE values for the "back" configuration undergo a further reduction over the visible wavelength range, suggesting that the thickness of the IZrO film on the n-side could be slightly different from the one on the p-side, hence resulting in a different – worse – optical response of the device as compared to that of the "front" configuration.

4. Conclusions

In summary, we grew Zirconium doped Indium Oxide thin films by co-sputtering deposition at room temperature followed by post-deposition thermal annealing at T = 200 °C. A preliminary study has been performed to determine the Zr content that optimizes the opto-electrical properties. Measurements show that, with Zr = 0.6 at.%, carrier mobility up to 21 $cm^2V^{-1}s^{-1}$ and optical transparency up to T = 86 % in the VIS range and T = 92 % in the NIR range can be achieved after annealing, thanks to an improvement of the crystalline quality of the films as confirmed by XRD measurements. In addition, the material

satisfies all the requirements for an excellent TE, such as uniform work function ($W_F \approx 4.6$ eV), wide bandgap ($E_g \approx 4$ eV), and low surface-roughness (1 nm < RMS <2 nm). With the aim to follow the In-based-TCO reduced thickness strategy, to reduce the amount of Indium without degrading the electrode performance, we set up a study as a function of the IZrO thickness. Three different samples were grown with decreasing thickness (90 nm, 40 nm, and 15 nm) and characterized through different techniques. The thinnest film of 15 nm was compared to other ultra-thin TCO films (ITO-20nm and AZO-20nm) showing the lowest Sheet Resistance ($R_{sh} = 344\ \Omega/\square$). Lastly, we also tested the EQE performances of 90 nm thick IZrO films as proof-of-concept standalone front and back contacts in SHJ bifacial solar cells. The results point out that IZrO works very well as TCO/a-Si(p+):H contact, being its EQE comparable to that of the commercial ITO-based SHJ solar cell, taken as a reference. On the other hand, IZrO contact on the a-Si(n+):H side didn't provide comparably good results, suggesting that the electronic properties of this material (and in particular its work function) are not ideal at the present stage. Even though the electronic properties of IZrO need to be optimized to effectively replace ITO as back contact, this work points out that optimized thickness and production process can make IZrO a promising alternative to ITO for application as a front contact in Silicon Heterojunction solar cells.

CRediT authorship contribution statement

Melanie Micali: Writing – original draft, Methodology, Investigation, Data curation. **Andrea Lo Mastro:** Writing – review & editing. **Fiorella Tringali:** Writing – review & editing. **Marco Leonardi:** Investigation, Data curation. **Salvatore Lombardo:** Writing – review & editing, Conceptualization. **Giuseppe Bengasi:** Writing – review & editing. **Claudio Colletti:** Writing – review & editing. **Marina Foti:** Writing – review & editing. **Esther Alarcón Lladó:** Writing – review & editing. **Maria Miritello:** Writing – review & editing. **Giorgia Franzò:** Writing – review & editing. **Antonio Terrasi:** Conceptualization, Formal analysis, Supervision, Writing – review & editing.

Declaration of competing interest

The authors declare that they have no known competing financial interests or personal relationships that could have appeared to influence the work reported in this paper.

Data availability

Data will be made available on request.

Acknowledgements

The authors acknowledge the important contribution of Giuseppe Panté, Salvatore Tatì and Carmelo Percolla of the CNR-IMM for technical skills. The work has been done in the framework and with the financial support of the project PRN DD n. 1735 BEST4U *"Bifacial Efficient Solar cell Technology with 4 terminal architecture for Utility scale"*.

Appendix A. Supplementary data

Supplementary data to this article can be found online at https://doi.org/10.1016/j.solmat.2024.112875.

References

[1] E. Ginley, S. David, Hideo Hosono, David C. Paine, Handbook of Transparent Conductors, 2010.
[2] C.G. Granqvist, Transparent Conductors as Solar Energy Materials: A Panoramic Review, vol. 91, North-Holland, 2007, pp. 1529–1598.
[3] M. Morales-Masis, S. De Wolf, R. Woods-Robinson, J.W. Ager, C. Ballif, Transparent Electrodes for Efficient Optoelectronics, vol. 3, Blackwell Publishing Ltd, 2017.
[4] David Levy, Erick Castellón (Eds.), Transparent conductive materials: materials, synthesis, characterization, applications, John Wiley & Sons, 2018, pp. 3–20.
[5] S. Sharma, S. Shriwastava, S. Kumar, K. Bhatt, C.C. Tripathi, Opto-Electron. Rev. 26 (2018) 223.
[6] D.S. Hecht, L. Hu, G. Irvin, Adv. Mater. 23 (2011) 1482.
[7] G. Torrisi, E. Cavaliere, F. Banfi, G. Benetti, R. Raciti, L. Gavioli, A. Terrasi, Sol. Energy Mater. Sol. Cells 199 (2019) 114.
[8] I. Crupi, S. Boscarino, G. Torrisi, G. Scapellato, S. Mirabella, G. Piccitto, F. Simone, A. Terrasi, Nanoscale Res. Lett. 8 (2013) 1.
[9] G. Torrisi, I. Crupi, S. Mirabella, A. Terrasi, Sol. Energy Mater. Sol. Cells 165 (2017) 88.
[10] S. Boscarino, I. Crupi, S. Mirabella, F. Simone, A. Terrasi, Appl. Phys. Mater. Sci. Process 116 (2014) 1287.
[11] S. Boscarino, M. Censabella, M. Micali, M. Russo, A. Terrasi, M.G. Grimaldi, F. Ruffino, mdpi.com (2022).
[12] F. Zhang, M. Johansson, M.R. Andersson, J.C. Hummelen, O. Inganäs, Adv. Mater. 14 (2002) 662.
[13] S. De, T.M. Higgins, P.E. Lyons, E.M. Doherty, P.N. Nirmalraj, W.J. Blau, J. J. Boland, J.N. Coleman, ACS Nano 3 (2009) 1767.
[14] G. Benetti, F. Banfi, E. Cavaliere, L. Gavioli, Mechanical Properties of Nanoporous Metallic Ultrathin Film: A Paradigmatic Case, vol. 11, Multidisciplinary Digital Publishing Institute, 2021, p. 3116.
[15] Z. Ren, J. Zhou, Y. Zhang, A. Ng, Q. Shen, S.H. Cheung, H. Shen, K. Li, Z. Zheng, S. K. So, A.B. Djurišić, C. Surya, Sol. Energy Mater. Sol. Cells 179 (2018) 36.
[16] S. Li, M. Pomaska, A. Lambertz, W. Duan, K. Bittkau, D. Qiu, Z. Yao, M. Luysberg, P. Steuter, M. Köhler, K. Qiu, R. Hong, H. Shen, F. Finger, T. Kirchartz, U. Rau, K. Ding, Joule 5 (2021) 1535.
[17] C. Han, R. Santbergen, M. van Duffelen, P. Procel, Y. Zhao, G. Yang, X. Zhang, M. Zeman, L. Mazzarella, O. Isabella, Prog. Photovoltaics Res. Appl. 30 (2022) 750.
[18] A. Cruz, D. Erfurt, P. Wagner, A.B. Morales-Vilches, F. Ruske, R. Schlatmann, B. Stannowski, Sol. Energy Mater. Sol. Cells 236 (2022) 111493.
[19] J. Xu, J.B. Liu, B.X. Liu, S.N. Li, S.H. Wei, B. Huang, Adv. Electron. Mater. 4 (2018) 1.
[20] Y.C. Liang, Y.C. Liang, Appl. Phys. Mater. Sci. Process 97 (2009) 249.
[21] E. Rucavado, F. Landucci, M. Döbeli, Q. Jeangros, M. Boccard, A. Hessler-Wyser, C. Ballif, M. Morales-Masis, Phys. Rev. Mater. 3 (2019) 084608.
[22] B. Aissa, Y. Zakaria, A.R. Shetty, A. Samara, C. Broussillou, Conf. Rec. IEEE Photovolt. Spec. Conf. 71 (2021).
[23] M. Morales-Masis, E. Rucavado, R. Monnard, L. Barraud, J. Holovsky, M. Despeisse, M. Boccard, C. Ballif, IEEE J. Photovoltaics 8 (2018) 1202.
[24] A. Jain, G. Hautier, C.J. Moore, S. Ping Ong, C.C. Fischer, T. Mueller, K.A. Persson, G. Ceder, Comput. Mater. Sci. 50 (2011) 2295.
[25] C. Guillén, J. Herrero, J. Appl. Phys. 101 (2007).
[26] C. Han, R. Santbergen, M. van Duffelen, P. Procel, Y. Zhao, G. Yang, X. Zhang, M. Zeman, L. Mazzarella, O. Isabella, Prog. Photovoltaics Res. Appl. 30 (2022) 750.
[27] J. Gwamuri, A. Vora, R.R. Khanal, A.B. Phillips, M.J. Heben, D.O. Guney, P. Bergstrom, A. Kulkarni, J.M. Pearce, Mater. Renew. Sustain. Energy 4 (2015) 1.
[28] J. Tauc, Amorphous and Liquid semiconductors, in: B.G. Bagleyauth (Ed.), Springer US, 1977 (Ed.: Media, S. S. & B.).
[29] S. Mirabella, R. Agosta, G. Franzó, I. Crupi, M. Miritello, R. Lo Savio, M.A. Di Stefano, S. Di Marco, F. Simone, A. Terrasi, J. Appl. Phys. 106 (2009).
[30] L. Martini, L. Serenelli, F. Menchini, M. Izzi, M. Tucci, Prog. Photovoltaics Res. Appl. 28 (2020) 235.